J. Fluid Mech. (1980), *vol.* 99, *part* 3, *pp.* 495–511
Printed in Great Britain

Theory and observations of waves on hollow-core vortices

By JAKOB J. KELLER AND M. P. ESCUDIER

Brown Boveri Research Centre,
CH-5405 Baden-Dättwil, Switzerland

(Received 8 June 1979 and in revised form 17 December 1979)

A linear non-homogeneous analysis is presented for the standing waves produced on the hollow core of an irrotational vortex by an arbitrary obstacle on the wall of the tube containing the vortex. The group-velocity criterion based upon Kelvin's corresponding dispersion relation predicts whether a certain asymptotic wave pattern appears upstream or downstream of the obstacle. The analysis leads to amplitude singularities for the standing waves at certain critical radii of the core. The particularly interesting case of a counter-helix for which the wave energy is propagating upstream appears for a first-mode angular disturbance. For this situation it seems to be possible that the helix ends in a hydraulic jump and is continued by a counter-helix downstream, as the core size gradually diminishes due to the deceleration of the flow caused by viscous effects (not included in the analysis). The capillary-wave pattern produced by surface tension is also considered. A brief outline for the analogous wave problem is given for the case where the fluid rotates like a rigid body.

Photographic observations of hollow-core vortices in water flow are presented which confirm the qualitative predictions of the analysis, both for the response to an axisymmetric area contraction and also to a 90° bend at the downstream end of the vortex tube.

1. Introduction

The present work was motivated by observations made in the course of experiments concerned with the structure of vortex flow in a jet-driven vortex tube (Escudier *et al.* 1980). At sufficiently high flow rates the pressure in the vortex core becomes low enough for cavitation to occur, the fluid medium being water. It was observed that, when the vortex so produced passes into a contraction, the diameter of the hollow core increases and the core surface develops a well-defined varicose wavy structure. The increase in core diameter, perhaps at first sight surprising, can be explained by elementary arguments (Escudier 1979). The wave behaviour on the other hand, which is analogous to that of surface gravity waves and therefore to be expected, is much more difficult to analyse.

The problem of wave propagation on a hollow irrotational vortex in a fixed cylindrical tube was first studied by Kelvin (1880). Using the Eulerian equations he derived the general dispersion relation for waves supported by centrifugal forces. A related problem was investigated by Binnie (1964), who considered waves on hollow swirling water jets, in which the surface tension and centrifugal forces balance. It is interesting to note that the dispersion relation derived by Binnie is, apart from a quadratic factor in the wavenumber, identical with Kelvin's dispersion relation for the special

0022-1120/80/4497-1590 $02.00

case of axial symmetry. The analysis of the present paper discusses standing waves produced on the free surface of the core of an irrotational vortex contained in a tube by a disturbance at the wall of the tube.

The diameter of the hollow core is determined by the cavitation pressure of the liquid which forms the vortex, or by the air pressure of a reservoir to which the vortex tube is connected. Assuming the flow to be irrotational and incompressible and ignoring effects due to the gas flow in the core the *standing*-wave pattern corresponding to a specified disturbance is calculated. For completeness the effects of surface tension are included, although in most cases they are of little importance.

The present *non-homogeneous* problem is closely related to that of standing gravity waves behind an obstacle in a river (see, for example, Whitham 1974). As the analysis given is linear, consideration is restricted to both small wave amplitudes and small disturbances at the wall. However, if an exact knowledge of the wave amplitudes is not needed, the second simplifying assumption can be dropped and it is then justified to apply the present ideas to the wave field behind a strong contraction or in front of a bend in the tube. As only asymptotic wave patterns are discussed, the radiation conditions have to be considered separately. Thus we can predict whether a certain wave pattern will appear upstream or downstream of an obstacle.

In the course of the development of the analysis, it became apparent that wave forms other than axisymmetric were to be expected for non-axisymmetric disturbances, and this was subsequently confirmed by experiment. Photographs are presented of the waves produced on hollow vortex cores by axisymmetric and non-symmetric disturbances, and wavelengths determined from the photographs are compared with the predictions of the analysis.

2. Analysis

It is convenient to assume a concentrated disturbance produced by the obstacle for the radial velocity at the wall in cylindrical co-ordinates (x, r, θ)

$$v_r(x, r_t, \theta) = \alpha u_0 \delta(x) \cos n\theta, \tag{1}$$

where δ is Dirac's delta function, u_0 the mean axial flow speed, n an integer, α a constant with an absolute value which is small compared with unity, and r_t the radius of the tube. This leads to a Green's function, from which the solution for a general disturbance

$$\int_{-\infty}^{+\infty} \delta(x-y) . \sum_{n=0}^{\infty} [g_n(y) \cos n\theta + h_n(y) \sin n\theta] \, dy \tag{2}$$

is found by superposition.

First, the equilibrium of the undisturbed flow must be examined. Since the motion is taken to be irrotational, the tangential velocity at radius r is given by $v_\theta = \Gamma/(2\pi r)$, where the circulation integral Γ is a constant. The outer radius of the vortex is equal to the radius of the tube r_t and the inner radius (i.e. the core radius) is denoted by r_c. Hence the velocity potential can be written in the form

$$\phi(x, r, \theta) = u_0 x + \frac{\Gamma}{2\pi} \theta + \chi(x, r, \theta), \tag{3}$$

where χ accounts now for the disturbance from the wall. To determine the boundary condition on the core we describe the free surface by $f(x,r,\theta) = \eta(x,\theta)+r_c-r = 0$. Making use of

$$v_x\frac{\partial f}{\partial x}+v_r\frac{\partial f}{\partial r}+\frac{v_\theta}{r}\frac{\partial f}{\partial \theta} = 0 \quad \text{on} \quad f(x,r,\theta) = 0, \tag{4}$$

we find, to first order in η,

$$u_0\frac{\partial \eta}{\partial x}+\frac{\Gamma}{2\pi r_c^2}\frac{\partial \eta}{\partial \theta}-\frac{\partial \chi}{\partial r} = 0 \quad \text{at} \quad r = r_c. \tag{5}$$

A second condition can be obtained from Bernoulli's equation

$$\frac{p_c}{\rho} = \frac{p_0}{\rho}-\frac{p_s}{\rho}-\tfrac{1}{2}(\nabla\phi)^2 = \text{const.} \quad \text{on} \quad f(x,r,\theta) = 0, \tag{6}$$

where p_0, p_c, p_s and ρ denote the stagnation pressure, the core pressure, the pressure due to surface tension and the density, respectively. Having determined the curvature of the free surface, we obtain to first order

$$p_s = -\rho\gamma\cdot\left\{\frac{1}{r_c}-\frac{\eta}{r_c^2}-\frac{\partial^2\eta}{\partial x^2}-\frac{1}{r_c^2}\frac{\partial^2\eta}{\partial\theta^2}\right\}+P_s, \tag{7}$$

where P_s is the pressure due to surface tension for the undisturbed case and γ the kinematic surface tension. Introducing (7) into (6) and equating the first-order terms in (6) leads to

$$u_0\frac{\partial \chi}{\partial x}+\frac{\Gamma}{2\pi r_c^2}\frac{\partial \chi}{\partial \theta}-\left(\frac{\Gamma^2}{4\pi^2 r c^3}-\frac{\gamma}{r_c^2}\right)\eta+\gamma\frac{\partial^2\eta}{\partial x^2}+\frac{\gamma}{r_c^2}\cdot\frac{\partial^2\eta}{\partial\theta^2} = 0 \tag{8}$$

at $r = r_c$.

The velocity-potential disturbance χ has to satisfy Laplace's equation

$$\Delta\chi = 0. \tag{9}$$

With this and the boundary conditions (1), (5) and (8) the problem is completely defined.

As pointed out by Whitham (1974), care is needed when solving steady wave problems by transforms in the application of a suitable radiation condition to ensure uniqueness. The non-uniqueness is a consequence of assuming a steady-state solution without regard for its evolution. A convenient technique to overcome this problem is to use the artifice of Whitham, whereby the steady-state problem is replaced by a time-dependent one, thereby introducing a causality requirement. Thus, in the present case the boundary condition (1) is replaced by

$$v_r(x,r_t,\theta;t) = \alpha u_0\delta(x)\cos n\theta\cdot\exp\left(\Delta\cdot\frac{u_0 t}{r_c}\right), \quad \Delta > 0. \tag{10}$$

This expression defines the more realistic problem of a source which was initially (i.e. at $t = -\infty$) effectively zero and gradually grew until it reached its current strength (at $t = 0$). Once this problem is solved, the limit $\Delta \to 0$ yields the steady-state solutions. Equations (5) and (8) are extended correspondingly to their time-dependent forms by simply adding the terms $\partial\eta/\partial t$ and $\partial\chi/\partial t$, respectively.

It is then easy to show that the appropriate forms for χ and η representing varicose disturbances are

$$\chi(x,r,\theta;t) = \exp\left(\Delta.\frac{u_0 t}{r_c}\right)\int_{-\infty}^{+\infty}\{[A(k)\,I_n(kr)+B(k)\,K_n(kr)]\,e^{in\theta}] + [C(k)\,I_n(kr)+D(k)\,K_n(kr)]\,e^{-in\theta}]\}\,e^{ikx}\,dk \quad (11)$$

and

$$\eta(x,\theta;t) = \frac{\exp\left(\Delta.\frac{u_0 t}{r_c}\right)}{iu_0}\int_{-\infty}^{+\infty}\{E(k)\,e^{in\theta}+F(k)\,e^{-in\theta}\}\,e^{ikx}\,dk. \quad (12)$$

For convenience we introduce the following substitutions

$$\beta = \frac{\Gamma}{2\pi r_c.u_0}, \quad \xi = |k|\,r_c, \quad (13), (14)$$

$$R = r_c/r_t, \quad z = x/r_c, \quad (15), (16)$$

$$\sigma(\xi) = \beta^2 + \frac{\gamma}{u_0^2 r_c}.[(n^2-1)+\xi^2]. \quad (17)$$

Note that σ is a constant when the effects due to surface tension can be ignored.

Introduction of (11) and (12) into the relations defining the boundary conditions leads to the transforms A, B, C, D, E and F. Inserting the solutions for E and F in (12), breaking the integral into the ranges $k > 0$ and $k < 0$ and using ξ as the variable of integration in each, we obtain

$$\eta(x,t) = \frac{\alpha.\exp\left(\Delta.\frac{u_0 t}{r_c}\right)}{4\pi i}.\sum_{j_1=\pm 1}\sum_{j_2=\pm 1}\int_0^{\infty} j_1\,\frac{[\xi+j_2 n\beta-j_1 i\Delta]\exp(j_1 i[\xi z+j_2 n\theta])\,d\xi/\xi}{\xi.\sigma W_n(\xi)+[\xi+j_2 n\beta-j_1 i\Delta]^2.V_n(\xi)}, \quad (18)$$

where

$$V_n(\xi) = I_n'(\xi/R).K_n(\xi)-K_n'(\xi/R)\,I_n(\xi), \quad (19)$$

$$W_n(\xi) = I_n'(\xi/R).K_n'(\xi)-K_n'(\xi/R)\,I_n'(\xi), \quad (20)$$

and use has been made of the symmetry relations

$$V_n(\xi) = -V_n(-\xi) \quad \text{and} \quad W_n(\xi) = W_n(-\xi).$$

The role of Δ is now clear. The fact that the imaginary parts appearing in the denominators of the integrands of the expression (18) are strictly different from zero excludes the possibility of singularities on the path of integration.

3. Dispersion relation

It is straightforward to introduce harmonic time dependence and to arrive at the dispersion relation

$$\left[-\frac{\omega/k}{u_0}\xi+j_2 n\beta\right]^2.V_n(\xi)+\sigma.\xi.W_n(\xi) = 0. \quad (21)$$

This is identical with Kelvin's dispersion relation when $\gamma = 0$ and, in the limit $\Delta \to 0$, is also identical with the denominators of the integrands on the right-hand side of (18) when $\omega/k = -u_0$. On the other hand this is just the phase-speed condition for standing waves

$$c \equiv \omega/k = -u_0, \quad (22)$$

i.e. for the only waves that can keep up with the obstacle at the wall of the tube and appear steady when viewed from a fixed position in the laboratory frame of reference. The group velocity is defined by $C = \partial\omega/\partial k$. From (21) we have

$$C/u_0 = -\frac{\partial}{\partial\xi}\left[-\sigma\xi\frac{W_n}{V_n}\right]^{\frac{1}{2}} \cdot \operatorname{sgn}\left(-\frac{c}{u_0}+\frac{j_2 n\beta}{\xi}\right), \tag{23}$$

where

$$\operatorname{sgn}(x) = \begin{cases} 1 & \text{if } x > 0, \\ 0 & \text{if } x = 0, \\ -1 & \text{if } x < 0. \end{cases}$$

When $c = u_0$ and $C > -u_0$ the wave pattern will appear downstream of the obstacle, whereas for $C < -u_0$ it will appear upstream. It is important to note that only the real roots of (22), i.e. in the limit $\Delta \to 0$ the real poles of the integrands of (18), contribute to the (far-field) asymptotic wave pattern. Everything else contributes only to the transitional behaviour of the wave field near the obstacle (near field).

4. Solutions

To show how solutions are constructed we consider first the case of an axisymmetric source. Since $\Delta \to 0$ ultimately, terms which have arisen from the time dependence of the boundary condition (10) and are no longer needed to evaluate the integrals in (18), can now be dropped. Thus if $n = 0$, equation (18) becomes

$$\eta(x) = \frac{\alpha}{2\pi i}\sum_{j=\pm 1}\int_0^\infty j\frac{e^{ji\xi z}\,d\xi/\xi}{\sigma W_0(\xi)+[\xi-2ji\Delta]V_0(\xi)}, \tag{24}$$

where

$$V_0(\xi) = I_0(\xi)K_1(\xi/R)+I_1(\xi/R)K_0(\xi),$$

$$W_0(\xi) = I_1(\xi)K_1(\xi/R)-I_1(\xi/R)K_1(\xi).$$

Having noted that $V_n(\xi)$ is strictly positive and $W_n(\xi)$ strictly negative if n is a non-negative integer, and that $0 < R < 1$ and $\xi > 0$, it is easy to see to which side of the real axis the poles of the integrands of (18) have been shifted into the complex plane due to the appearance of Δ. In this section we exclude consideration of capillary waves, and to avoid unnecessary complications set $\gamma = 0$. In this case the dispersion relation which corresponds to the denominators of the integrands in (24) has exactly one (simple) zero

$$\xi = \xi_0(R,\beta) \tag{25}$$

if

$$R < R_c(\beta) \tag{26}$$

and no zero otherwise; here R_c is a critical ratio of radii. The corresponding pole of the first integrand ($j = +1$) in (24) appears in the upper complex half-plane (i.e. with positive imaginary parts of ξ) and the pole of the other integrand ($j = -1$) is in the lower half-plane. The paths of the two integrals can now be rotated into the upper and the lower half-planes, respectively, such that no poles appear in the integrands. Thus both poles corresponding to the zero (25) contribute and the remaining parts of the integrals decay exponentially as $z \to \infty$ and are now neglected as we are interested only in the asymptotic behaviour of the solutions (far field). The asymptotic solution is

$$\eta(x) = 2\alpha a\cos\left(\xi_0\cdot\frac{x}{r_c}\right), \tag{27}$$

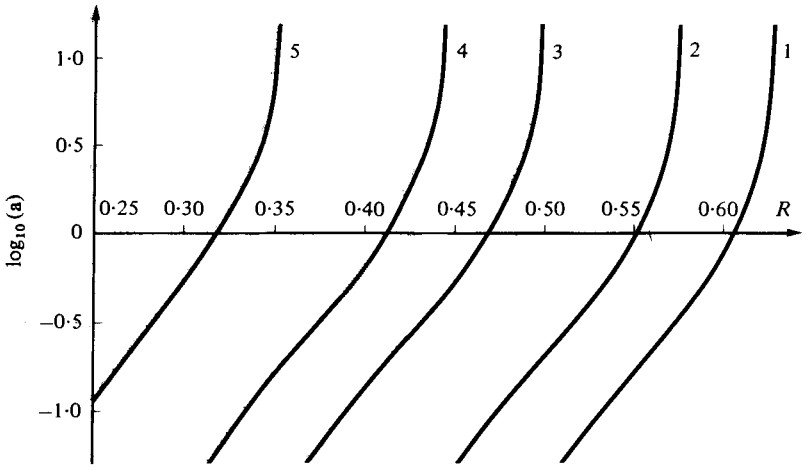

FIGURE 1. Logarithm of the relative wave amplitude **a** *versus* the ratio of radii R for $n = 0$ and the following values of κ (defined by equation (30)): 1, 1·208; 2, 0·879; 3, 0·549; 4, 0·396; 5, 0·220.

where
$$a = \lim_{\xi \to \xi_0} \frac{\xi - \xi_0}{\xi[\beta^2 W_0(\xi) + \xi V_0(\xi)]}, \tag{28}$$

which represents a sinusoidal chain of cells. For consistency with the experimental study, we consider the specific case of a hollow-core vortex produced by a tangential inlet at the upstream end of the vortex tube. Thus, making use of the continuity equation, it is easy to see that for a fixed geometry

$$\beta \sim \frac{1 - R^2}{R}. \tag{29}$$

Hence the parameter for the solutions should be

$$\kappa = \frac{R}{1 - R^2} \cdot \beta. \tag{30}$$

The relative amplitude **a** versus the ratio of radii R is shown in figure 1 for five different values of κ, which correspond to the parameters chosen for the experiment plus the limiting case of an infinitesimal disturbance. The corresponding values of $\xi = \xi_0$ are plotted in figure 2. Finally the group velocity C is shown in figure 3. It is interesting to note that, when R approaches R_c, ξ approaches zero (i.e. the wavelength becomes infinitely long), the amplitude **a** becomes infinitely large and C approaches $-u_0$. It is not surprising that the amplitude becomes very large as $C \to -u_0$, because in this case the wave energy produced is trapped in place. As the present analysis is *linear* and does not account for dissipative mechanisms it predicts a singularity for **a** which should be interpreted in the same way as the usual amplitude singularity in a resonance problem.

The case $n = 1$ can be discussed similarly. The theory again leads to a critical ratio of radii R_c. For $R > R_c$ the integrands of the first two integrals in (18) (i.e. $j_1 = \pm 1$, $j_2 = +1$) contain two poles each, corresponding to the two zeros of the dispersion relation (21) for $j_2 = +1$, and for $R > R_c$ these integrands are regular. The integrands

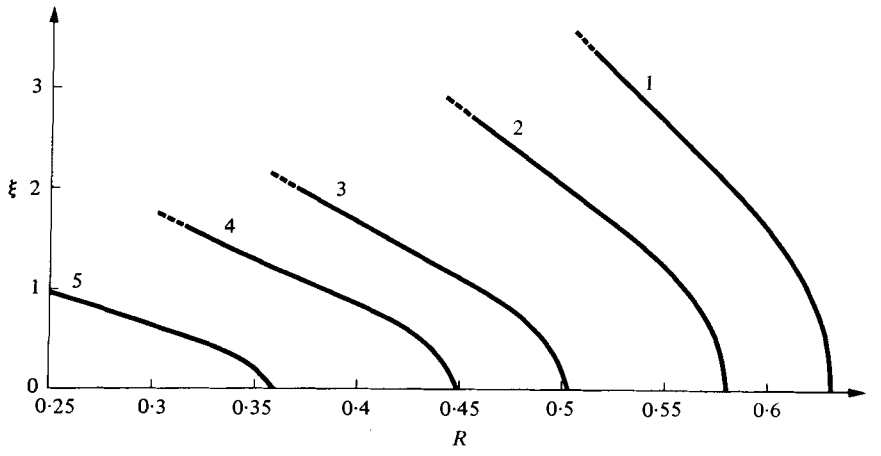

FIGURE 2. Relative wavenumber ξ (defined by equation (14)) *versus* R for $n = 0$ and the same values of κ as in figure 1.

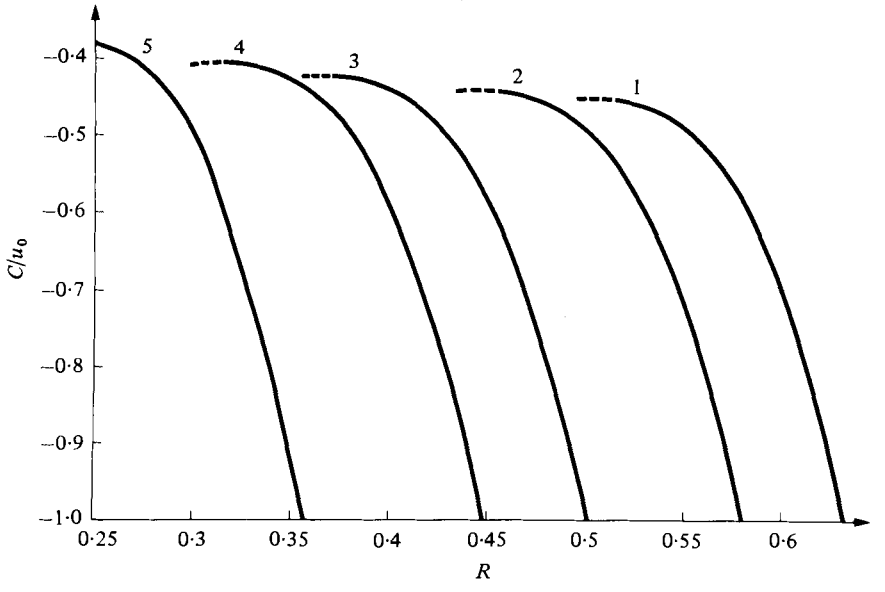

FIGURE 3. Ratio of group velocity and flow speed *versus* R for $n = 0$ and the same values of κ as in figure 1.

of the second two integrals (i.e. $j_1 = \pm 1$, $j_2 = -1$) contain two such poles for all values of R; both pairs of poles contribute. Consequently, we find

$$\eta_2(x, \theta) = 2\alpha . \left\{ a_{21} \cos\left(\xi_{21} \frac{x}{r_c} - \theta \right) + a_{22} \cos\left(\xi_{22} \frac{x}{r_c} - \theta \right) \right\} \tag{31}$$

for the asymptotic wave pattern, provided $R > R_c$. This represents a superposition of two helices. The group velocity criterion shows again that both of the waves which correspond to the terms on the right-hand side of (31) appear downstream of the

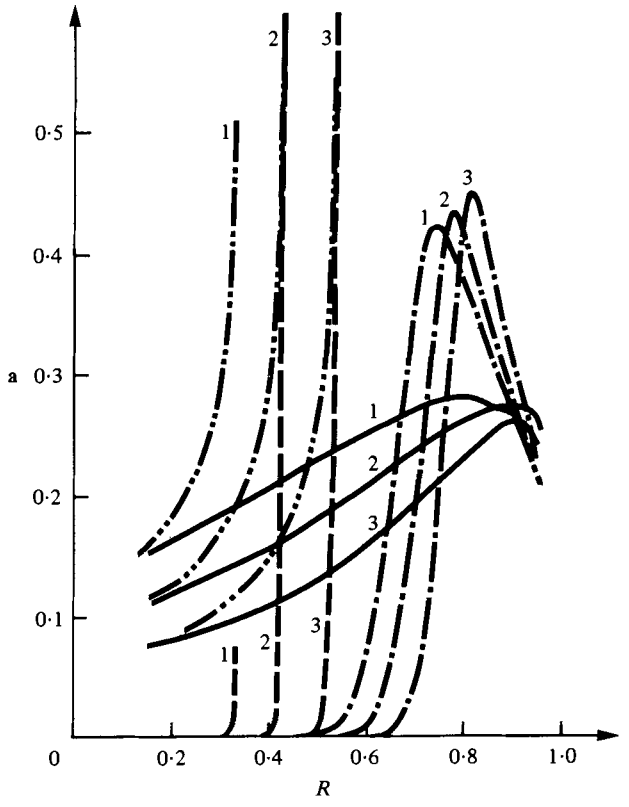

FIGURE 4. Relative wave amplitude **a** *versus* R for $n = 1$ and the following values of κ: 1, 1·208; 2, 1·692; 3, 2·538. The four solution branches are: —··—··, a_{11}; – – – – –, a_{12}; ——, a_{21}; —·—, a_{22}.

obstacle (for all values of R). When $R < R_c$ two additional waves appear. The one with the longer wavelength appears upstream of the obstacle, the other downstream. Hence, we have

$$\eta(x,\theta) = -2\alpha a_{11}\cos(\xi_{11}x/r_c+\theta) \quad \text{upstream}, \tag{32}$$

and

$$\eta(x,\theta) = 2\alpha a_{12}\cos(\xi_{12}x/r_c+\theta)+\eta_2(x,\theta) \quad \text{downstream}. \tag{33}$$

Expression (32) represents a pure counter-helix whereas (33) is a superposition of a counter-helix and two helices. The quantities **a**, ξ and C versus R are shown in figures 4, 5 and 6, respectively. Similar amplitude singularities as were observed previously now appear for a_{11} and a_{12}. Again in both cases the corresponding group velocities approach $-u_0$ as $R \to R_c$.

For the special case $n = 0$ it is possible to find an analytical relation between β and the critical ratio of radii. Resonance occurs when the dispersion relation (21) (for $n = 0$) contains a second-order (or higher-order) zero at $\xi = 0$. It is easy to show that this can only happen if

$$\beta = R.\left(\frac{2}{1-R^2}\right)^{\frac{1}{2}}.$$

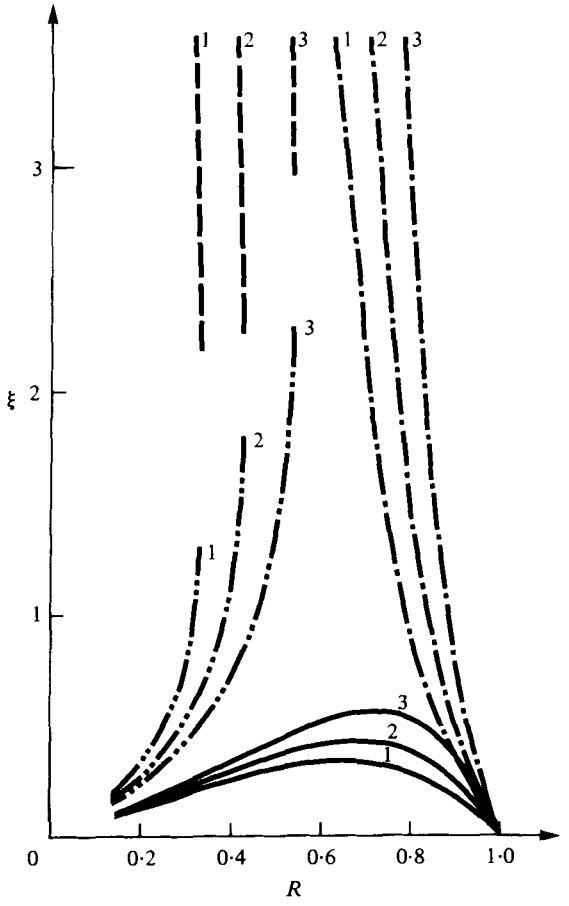

FIGURE 5. Relative wavenumber ξ *versus* R for $n = 1$ and the same solution branches and values of κ as in figure 4.

Hence we obtain from (12) and (14)

$$\frac{\Gamma}{2\pi r_t . u_0} = R_c^2 . \left(\frac{2}{1-R_c^2}\right)^{\frac{1}{2}}, \tag{34}$$

which is in agreement with the numerical results, and introducing (34) in (23) leads to $C = u_0$.

A similar simplification is possible for capillary waves as is seen in the following section.

5. Capillary waves

Capillary waves appear owing to surface tension. The dispersion relation (21) shows that their wavelengths are usually very small as the kinematic surface tension for most liquids is low (e.g. for water: $\gamma = 7{\cdot}4 \times 10^{-5}$ m^3 s^{-2}). Hence, we have approximately, using the asymptotic forms of the modified Bessel functions,

$$V_n(\xi) = \frac{R^{\frac{1}{2}}}{\xi} \cosh\left(\xi \frac{1-R}{R}\right) \tag{35}$$

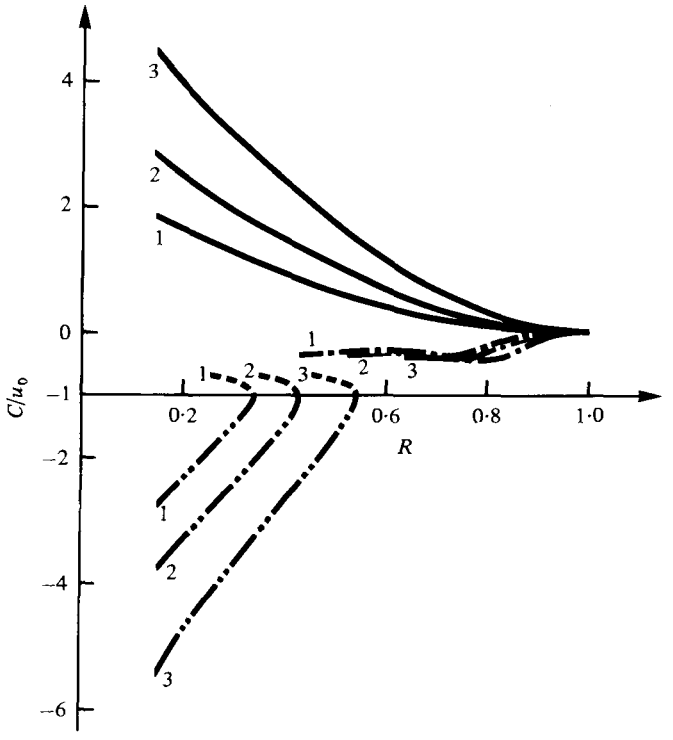

FIGURE 6. Ratio of axial group velocity and flow speed *versus* R for $n = 1$ and the same solution branches and values of κ as in figure 4.

and
$$W_n(\xi) = -\frac{R^{\frac{1}{2}}}{\xi}\sinh\left(\xi\frac{1-R}{R}\right). \tag{36}$$

The dispersion relation (21) simplifies to

$$\left[-\frac{c}{u_0}+\frac{j_2 n\beta}{\xi}\right]^2 = \frac{\gamma}{u_0^2 . r_c}.\xi.\tanh\left(\xi\frac{1-R}{R}\right). \tag{37}$$

From (18) we see that the amplitudes of the standing capillary waves are particularly large when $1-R \ll 1$. When (37) is multiplied by ξ^2 and differentiated with respect to ξ we obtain

$$2\left[-\frac{\xi c}{u_0}+j_2 n\beta\right].\left[-\frac{C}{u_0}\right] = \frac{\gamma}{u_0^2 r_c}.\left\{3\xi^2\tanh\left(\xi\frac{1-R}{R}\right)+\xi^3\frac{1-R}{R}\left[1-\tanh^2\left(\xi\frac{1-R}{R}\right)\right]\right\}.$$

This shows that any capillary-wave pattern will appear upstream of the obstacle only, provided

$$n < \xi/3\beta. \tag{38}$$

When $n \ll \xi/\beta$ and $\xi(1-R)/R \gg 1$ the wavenumber is given approximately by

$$k = u_0^2/\gamma. \tag{39}$$

6. Rotation as a rigid body

The only simple case of vortical flow which can be discussed in a similar manner to the irrotational vortex is that where in the undisturbed case the fluid rotates as a rigid body and moves at uniform axial speed, i.e. the undisturbed flow is defined by

$$v_x = u_0 = \text{const.}, \quad v_r = 0,$$

and

$$v_\theta = \Omega r \quad \text{for} \quad r_c < r < r_t. \tag{40}$$

As the flow is no longer irrotational, the velocity components cannot be expressed as derivatives of a velocity potential. However, Batchelor (1967, § 7.5) has derived an equation for the stream function for axisymmetric flow which can be used instead of Laplace's equation for the velocity potential:

$$\frac{\partial^2 \Psi}{\partial x^2} + \frac{\partial^2 \Psi}{\partial r^2} - \frac{1}{r}\frac{\partial \Psi}{\partial r} = \frac{2\Omega^2}{u_0} r^2 - \frac{4\Omega^2}{u_0^2}\Psi, \tag{41}$$

where

$$v_x = \frac{1}{r}\frac{\partial \Psi}{\partial r}, \quad v_r = -\frac{1}{r}\frac{\partial \Psi}{\partial x}. \tag{42}$$

Following Batchelor we use the departure of the stream function from its undisturbed form as the dependent variable

$$\Psi(x, r) = \tfrac{1}{2} u_0 r^2 + rF(x, r). \tag{43}$$

When this is introduced into (41) we obtain

$$\frac{\partial^2 F}{\partial x^2} + \frac{\partial^2 F}{\partial r^2} + \frac{1}{r}\frac{\partial F}{\partial r} + \left(\frac{4\Omega^2}{u_0^2} - \frac{1}{r^2}\right) F = 0. \tag{44}$$

In addition to the previous substitutions we define

$$\beta = \Omega r_c / u_0, \tag{45}$$

$$\xi_- = (4\beta^2 - \xi^2)^{\frac{1}{2}}, \tag{46}$$

$$\xi_+ = (\xi^2 - 4\beta^2)^{\frac{1}{2}}. \tag{47}$$

As the flow is assumed to be axisymmetric the boundary condition (1) is reduced to

$$v_r = \alpha u_0 \delta(x) \quad \text{at} \quad r = r_t,$$

and the conditions (5) and (8) on the free surface of the hollow core have to be replaced by

$$u_0 \frac{\partial \eta}{\partial x} + \frac{\partial F}{\partial x} = 0 \quad \text{at} \quad r = r_c \tag{48}$$

and

$$u_0 \left(\frac{1}{r_c} F + \frac{\partial F}{\partial r}\right) - \Omega^2 r_c \eta = 0 \quad \text{at} \quad r = r_c, \tag{49}$$

respectively. Following all the steps of the previous analysis leads to the solution

$$\eta(x) = \frac{2\alpha}{\pi^2} \cdot \int_0^{2\beta} \frac{\sin(\xi z) \cdot d\xi/\xi}{J_1(\xi_-/R) \cdot [\xi_- \cdot Y_0(\xi_-) + \beta^2 Y_1(\xi_-)] - Y_1(\xi_-/R) \cdot [\xi_- \cdot J_0(\xi_-) + \beta^2 J_1(\xi_-)]}$$
$$+ \frac{\alpha}{\pi} \int_{2\beta}^{\infty} \frac{\sin(\xi z) \cdot d\xi/\xi}{I_1(\xi_+/R) \cdot [\xi_+ \cdot K_0(\xi_+) - \beta^2 K_1(\xi_+/R)] + K_1(\xi_+/R) \cdot [\xi_+ \cdot I_0(\xi_+) + \beta^2 I_1(\xi_+)]} \tag{50}$$

for the displacement of the surface, whereby the interpretation of these integrals should be such that all poles on the positive real axis contribute. Note that (50) has essentially the same form as (18) for the axisymmetric case $n = 0$. The discussion of this result is similar to that already given for the irrotational vortex and is therefore not repeated. An interesting difference, however, is the fact that resonance now appears at finite wavelengths.

The dispersion relations are

$$\omega^2 k_-[J_1(k_-r_t)\,Y_0(k_-r_c) - J_0(k_-r_c)\,Y_1(k_-r_t)] + (k\Omega)^2 r_c[J_1(k_-r_t)\,Y_1(k_-r_c) - J_1(k_-r_c)\,Y_1(k_-r_t)] = 0 \quad (51)$$

if $\omega > 2\Omega$,

and

$$\omega^2 k_+[I_1(k_+r_t)\,K_0(k_+r_c) + I_0(k_+r_c)\,K_1(k_+r_t)] - (k\Omega)^2 r_c[I_1(k_+r_t)\,K_1(k_+r_c) - I_1(k_+r_c)\,K_1(k_+r_t)] = 0 \quad (52)$$

if $\omega < 2\Omega$;

where
$$k_- = [1 - (2\Omega/\omega)^2]^{\frac{1}{2}}.k \quad (53)$$

and
$$k_+ = [(2\Omega/\omega)^2 - 1]^{\frac{1}{2}}.k. \quad (54)$$

In this context reference should be made to the extensive work on inertia waves presented by Greenspan (1968) and Batchelor (1967), which is closely related to the present problem.

7. Concluding remarks regarding the analysis

As the present analysis is linear and for the most part neglects viscous effects, its application is restricted in several respects. In order to keep the angular shear stress of the undisturbed flow within appropriate limits (to produce approximately potential flow) the value of R should not be too small. On the other hand, as was mentioned in the first section, the wave amplitudes should not be too large, a restriction which is particularly important when R is close to a critical ratio of radii. In this context a very interesting aspect of the viscous flow should be discussed briefly. Due to boundary-layer friction at the wall, we expect the flow to be decelerated downstream. Consequently, the core radius should diminish in the downstream direction. In this case it is possible that

$$R > R_c \quad \text{for} \quad x < x_c$$

and
$$R < R_c \quad \text{for} \quad x > x_c,$$

where $x = x_c$ refers to the axial position where the critical ratio of radii is reached. For the special case $n = 1$ there is the possibility that a helix going with the flow (η_2) appears for $x < x_c$ and a helix going against the flow (counter-helix: η_{11}) for $x > x_c$.

Thus, wave energy would propagate upstream for $x < x_c$. Consequently, a very strong dissipative mechanism has to balance the energy flow coming from both sides towards x_c and it is anticipated that a hydraulic jump will appear at x_c.

Another interesting feature of waves supported by centrifugal forces is the fact that η contains the ratio of velocity components β as a parameter only (see equation (24)) and not the actual velocities, whereas for capillary waves the absolute values of the velocity components are important. Hence, it is possible to distinguish the two

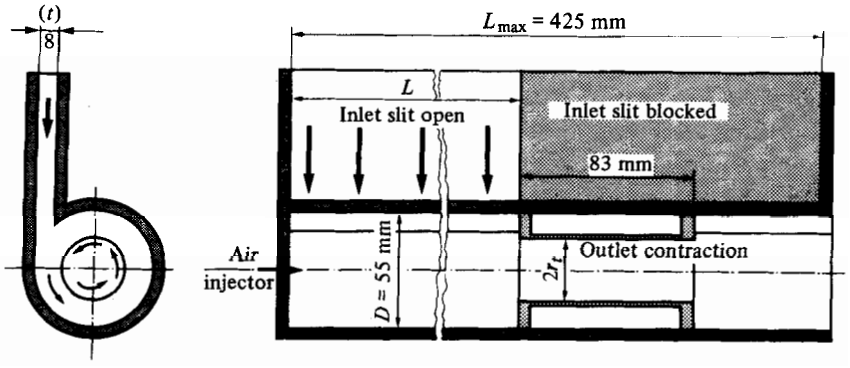

FIGURE 7. Schematic diagram of vortex tube.

types of waves experimentally. When β is kept constant, high-velocity flow produces capillary waves with small wavelengths, and with diminishing flow speed the wavelengths increase. Waves supported by centrifugal forces on the other hand do not change their lengths when β remains unchanged. Even though there are cases where we cannot expect good agreement of the amplitudes predicted by the present analysis with experimental data, the amplitude information is still very valuable, as it predicts at least the domains of R where reasonably large amplitudes are to be expected. Finally, it should be noted that boundary condition (1) represents approximately a sudden contraction of the tube for $n = 0$ and a sudden displacement of its axis for $n = 1$.

8. Flow apparatus

The flow apparatus employed for the experiments is shown schematically in figure 7. A vortex flow is created as the result of tangential inflow of water into the main vortex tube. This Plexiglas tube, together with an inlet header and a contraction upstream of the inlet slit, form part of a gravity-fed water circuit in which for the present experiments the flow is recirculated. The maximum attainable flow rate is typically a few litres per second, but varies with the geometric configuration under investigation, and may be regulated by valves upstream and downstream of the vortex tube.

The tube diameter $D = 55$ mm, and the inlet slit has a width $t = 8$ mm and an open length L which can be varied up to a maximum of 425 mm. Plexiglas exit contractions 83 mm in length and with inside diameters $2r_t = 40$, 25, 18 and 10 mm can be installed at any axial location within the tube (see figure 7), so producing an essentially axisymmetric disturbance to the vortex flow. Although some asymmetry results from the tangential inlet slit, this turns out to be of minor significance for the experiments with these outlet contractions, where the area change is between 47 % and 97 %. The response of the vortex to a strongly asymmetric disturbance in the form of a 90° elbow at the tube outlet is also investigated.

Except for the case with the 10 mm contraction installed, a hollow vortex core is always produced in our apparatus at the highest flow rates by gaseous cavitation, the water used having a relatively high air content. Such a core can also be produced under most flow conditions (including $2r_t = 10$ mm) by injecting air into the flow through a hole at the centre of the end wall of the vortex tube. For very low flow rates

this is no longer possible as the core breaks up under the buoyancy forces which then dominate. With air injection, the diameter of the core can be varied as desired, a smaller equilibrium value being reached when the air supply is shut off owing to gradual expulsion of the excess air.

Illumination for the photographs is provided by diffuse reflexion of the light of two flashguns from a white screen behind the tube, thereby achieving short exposure times and avoiding spurious reflexions whilst at the same time leaving the inner boundary of the hollow core clearly visible. For the camera set-up employed here, refraction at the outer surface of the vortex tube results in the core diameter appearing to be about 25 % larger than is actually the case.

9. Experimental results

(*a*) *Axisymmetric disturbance – contraction*

The response of hollow vortex cores to the various contractions is shown by the photographs in figures 8 to 11 (plates 1–4). In each case, the photographs cover a range of core diameters. The thick vertical band to the left marks the start of the contraction and the slender vertical ellipse at the right the outlet to the plenum chamber. The wavy surface produced by such a contraction is seen to be essentially varicose in shape with a slight helicity in the same sense as that of the outer swirling flow. Especially for the two smaller contractions, both the wavelength and the wave amplitude increase strongly with increase in the core diameter, until a limiting (or critical) size is reached at which the wavelength is so long that the core in the contraction is essentially cylindrical. For $2r_t = 25$ and 40 mm, photographs are shown for both maximum and reduced flow rates, the only difference being in the appearance of the core surface which changes from rough to smooth as the flow rate is reduced. This effect is consistent with the corresponding increase in the wavelength of the capillary waves, as discussed in § 5.

Data for the wavelength–core-size relationship, deduced from numerous photographs similar to those of figures 8 to 11, are plotted in figure 12 together with curves representing the predictions of the analysis (figure 2). The values of the parameter κ for $2r_t = 40$, 25, 18 and 10 mm are 0·88, 0·55, 0·40 and 0·22, respectively and correspond to the values associated with curves 2, 3, 4, and 5 of figure 2, respectively. Qualitative agreement of the observations discussed above is clearly evident in spite of systematic deviations between the data and the theoretical curves and also a high degree of scatter in the data themselves. The most obvious tendency for a given core diameter is for the computed wavelength to be shorter than observed, a trend which becomes the more pronounced as r_t is decreased. The explanation for this discrepancy may lie in the fact that the hollow core is surrounded by a sheath of turbulent fluid in almost solid-body rotation (Escudier *et al.* 1979) rather than potential-vortex flow as assumed in the analysis. It is also the case that for $2r_t = 40$ mm the contraction is rather short compared to the wavelength so that measurements can only be made in the 'near field' where application of the analysis is of doubtful value (nevertheless, the closest agreement between the theory and the measurements is for $2r_t = 40$ mm). It is also evident from the photographs that the wave amplitudes are much larger in most cases than is appropriate for comparison with a linear theory.

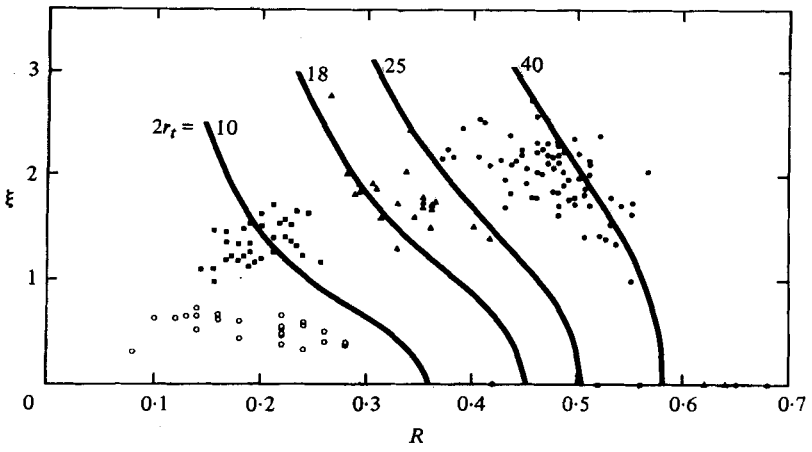

FIGURE 12. Wavelength–core-size relationship for axisymmetric disturbances. Solid curves from the analysis for values of exit diameter $2r_t$ indicated. Experimental data correspond to the exit diameters: ○, 10 mm; ■, 18 mm; ▲, 25 mm; ●, 40 mm.

(*b*) *Asymmetric disturbance – 90° elbow*

The series of photographs in figure 13 (plate 5) shows the appearance of the vortex core for maximum flow (5·2 l s^{-1}) through the vortex tube fitted with a 90° elbow at its downstream end. The pieces used to block off the downstream part of the inlet slit give the appearance of a step in the tube wall in figures 13 to 15. In fact the circular contour of the tube is faithfully maintained throughout. It may also be noted that these figures cover the full length (425 mm) of the tube. As the rate of air injection is reduced, a clear progression is evident from a large-diameter, more or less cylindrical, core on the surface of which capillary waves are seen, to a thin helical core. As suggested by the analysis, the sense of the helix (wave type 1, 1, i.e. the a_{11} solution) is opposite to that of the outer swirling flow (this anti-helical wave structure corresponds to the waves of largest amplitude in figure 4). It is also seen, as was again to be expected from the analysis, that the reduction in core diameter with downstream distance has important consequences for the flow, since the group velocity may exceed the axial flow speed, when the core becomes sufficiently small, thereby permitting wave energy to propagate upstream. This phenomenon leads to a form of hydraulic jump, as seen in figure 13(*b*)–(*e*), where according to the analysis wave energy from upstream and downstream is dissipated at the location of a critical core diameter.

The photographs in figure 14 (plate 6) are for a reduced flow rate of 2·0 l s^{-1}, the conditions otherwise being the same as those for figure 13. Except for the smoother appearance of the core surface, again corresponding to the appropriately longer wavelength of the capillary waves, there is no essential difference between the two series of photographs.

The photographs of figure 15 (plate 7) are for an inlet slit 100 mm in length (and again with the 90° elbow at the tube outlet) corresponding to $\kappa = 2{\cdot}54$ (compared with 1·21 for figures 13 and 14). This set-up has the practical advantage of yielding a longer length of tube in which to observe not only the main anti-helical wave structure but also the superimposed helical waves (type 2,1) of much longer wavelength – evident, for example, in figure 15(*d*).

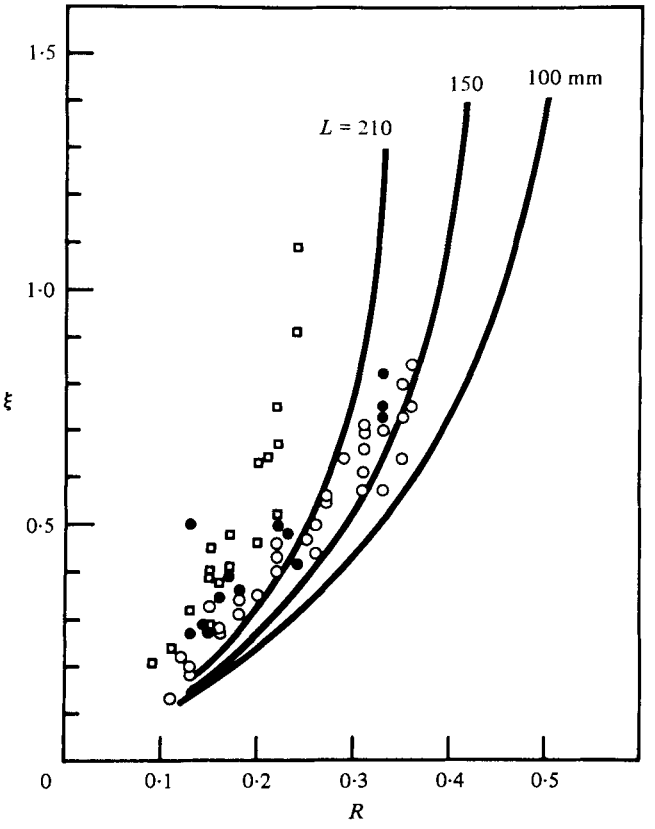

FIGURE 16. Wavelength–core-size relationship for asymmetric disturbances. Solid curves from the analysis for values of inlet-slit length L indicated. Experimental data correspond to the slit lengths: □, 210 mm; ●, 150 mm; ○, 100 mm.

There is again good qualitative agreement between these observations of the anti-helical waves and the analysis, as seen in figure 16 in which the wavelength–core-size relationship is examined. Data for $\kappa = 1{\cdot}21$, $1{\cdot}69$ and $2{\cdot}54$ are plotted, corresponding to curves 1, 2 and 3 respectively. The very short wavelength waves (type 1, 2) predicted by the analysis could not be distinguished in the photographs, probably through being masked by the longer wavelength, larger amplitude (except near the critical core radius) waves of type 1, 1. There is some indication of small amplitude waves with a wavelength comparable to the core diameter for the largest cores (see, for example, figures 13*a*, 14*a* and 15*a*) which could belong to type 2, 2. However, only waves of type 1, 1 could be identified unambiguously and therefore only data for this type are compared with the analysis. In this case, the data confirm both the general shape of the ξ–R curves and also the trend with κ.

The authors gratefully acknowledge the assistance of Mr N. Zehnder in performing the experiments and of Miss A. L. Larsen in printing numerous photographs for analysis.

REFERENCES

BATCHELOR, G. K. 1967 *An Introduction to Fluid Dynamics*. Cambridge University Press.

BINNIE, A. M. 1964 Annular Borda flow. *J. Fluid Mech.* **19**, 187–192.

ESCUDIER, M. P. 1979 Estimation of pressure loss in ring-type exit chambers. *Trans. A.S.M.E.* I, *J. Fluids Engng* **101**, 511–516.

ESCUDIER, M. P., BORNSTEIN, J. & ZEHNDER, N. 1980 Observations and LDA measurements of confined turbulent vortex flow. *J. Fluid Mech.* **98**, 49–63.

GREENSPAN, H. P. 1968 *The Theory of Rotating Fluids*. Cambridge University Press.

KELVIN, LORD 1880 Vibrations of a columnar vortex. *Phil. Mag.* **10** (5), 155–168. (*Math. and Phys. Papers* **4**, 152–171.)

WHITHAM, G. B. 1974 *Linear and Nonlinear Waves*. Wiley.

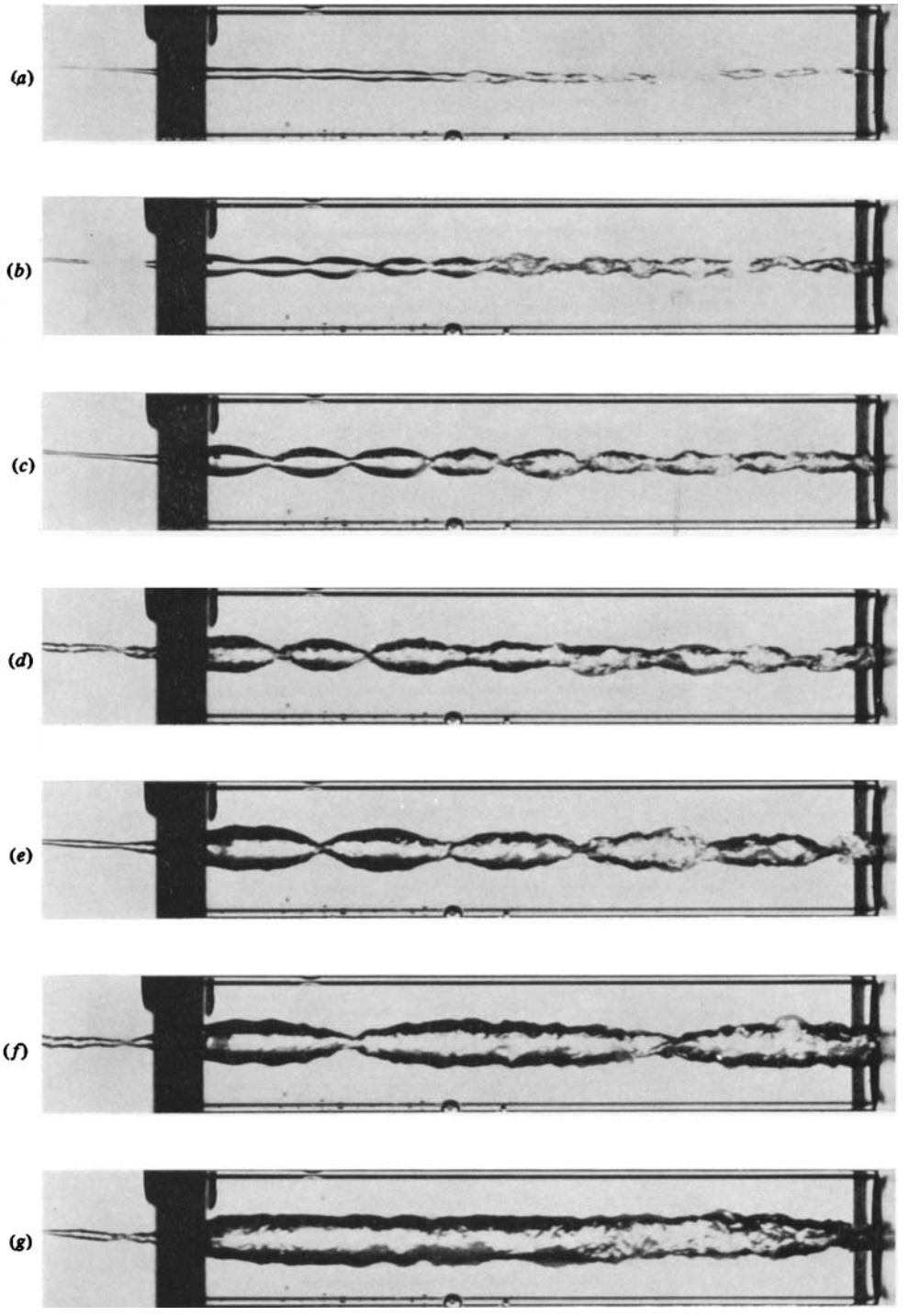

FIGURE 8. Photographs of hollow vortex core in 10 mm contraction; flow rate is 0·67 l s^{-1}.

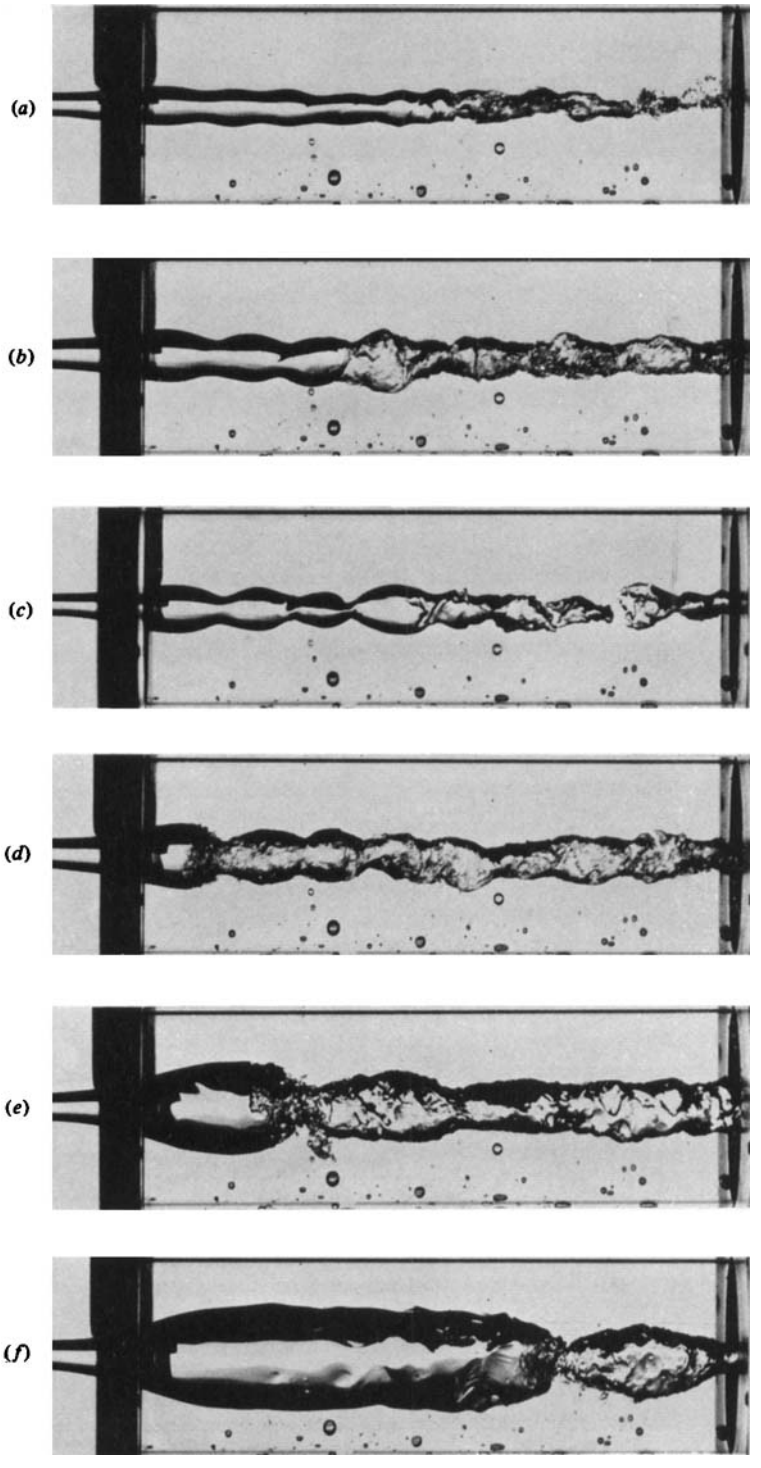

FIGURE 9. Photographs of hollow vortex core in 18 mm contraction; flow rate is 1·8 l s^{-1}.

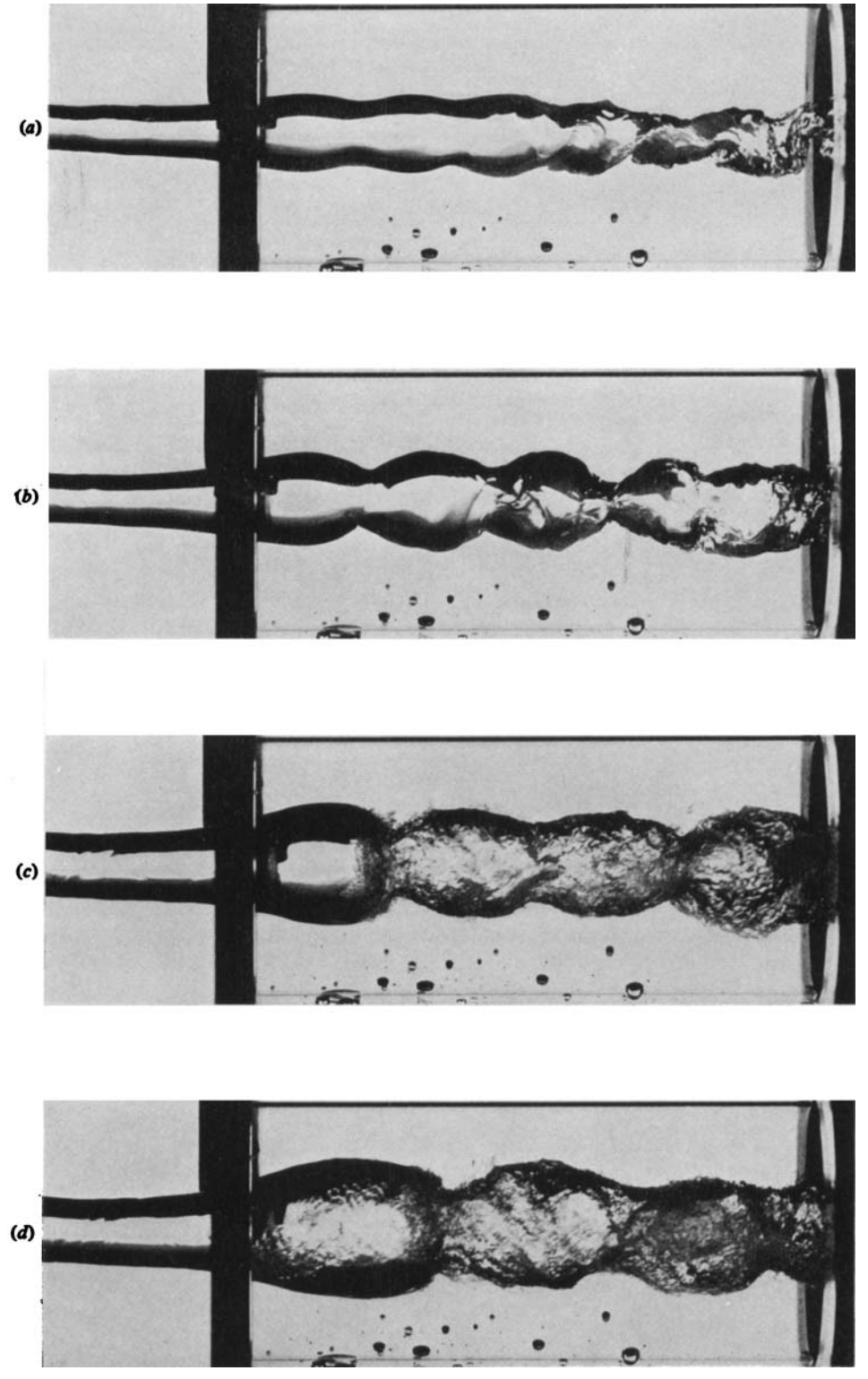

FIGURE 10. Photographs of hollow vortex core in 25 mm contraction.
Flow rates are: (*a*) 0·8 l s^{-1}; (*b*) 1·04 l s^{-1}; (*c*) 2·8 l s^{-1}; (*d*) 2·7 l s^{-1}.

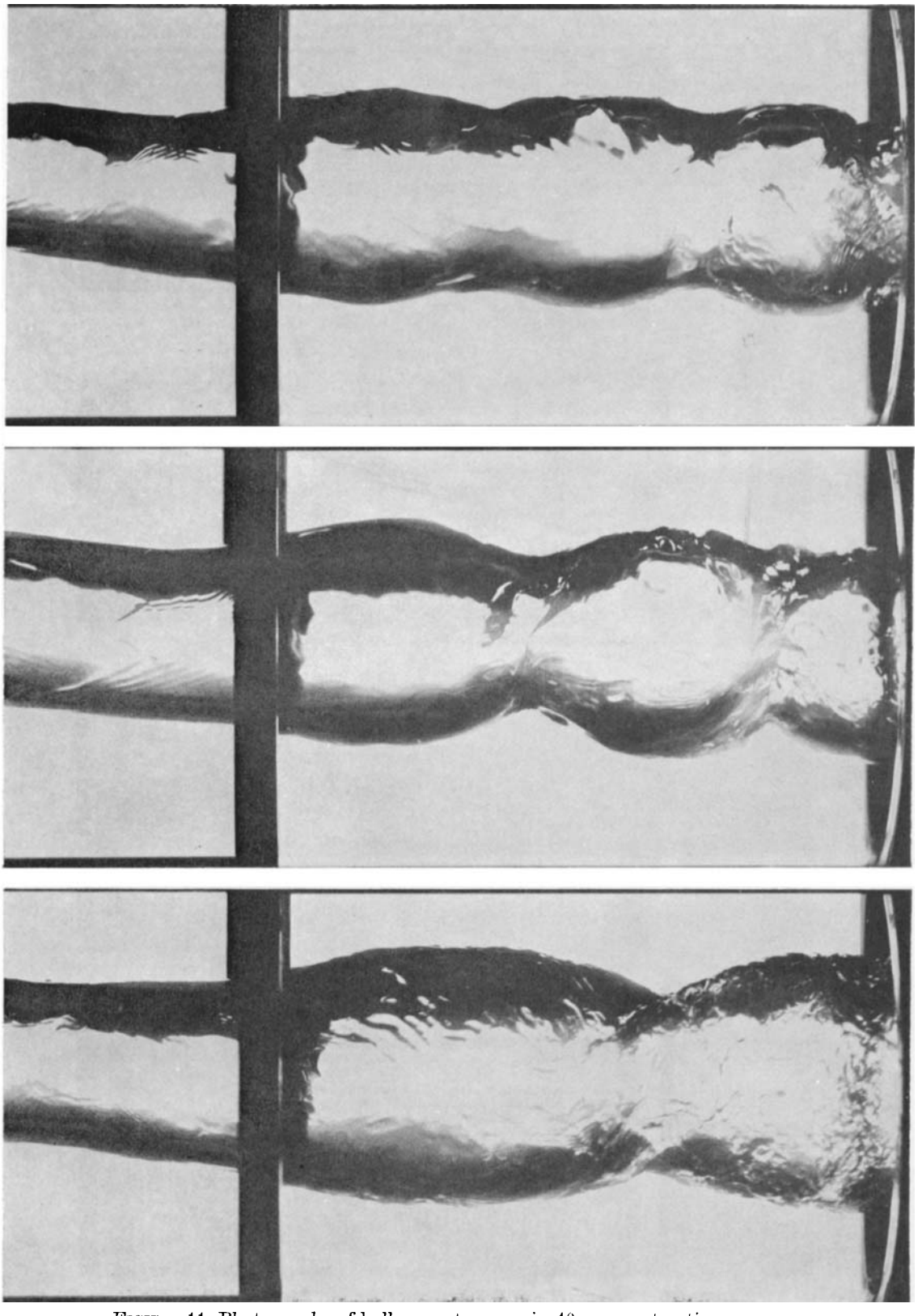

FIGURE 11. Photographs of hollow vortex core in 40 mm contraction.
Flow rates are: (*a*) 2·8 l s^{-1}; (*b*) 2·8 l s^{-1}; (*c*) 4·9 l s^{-1}.

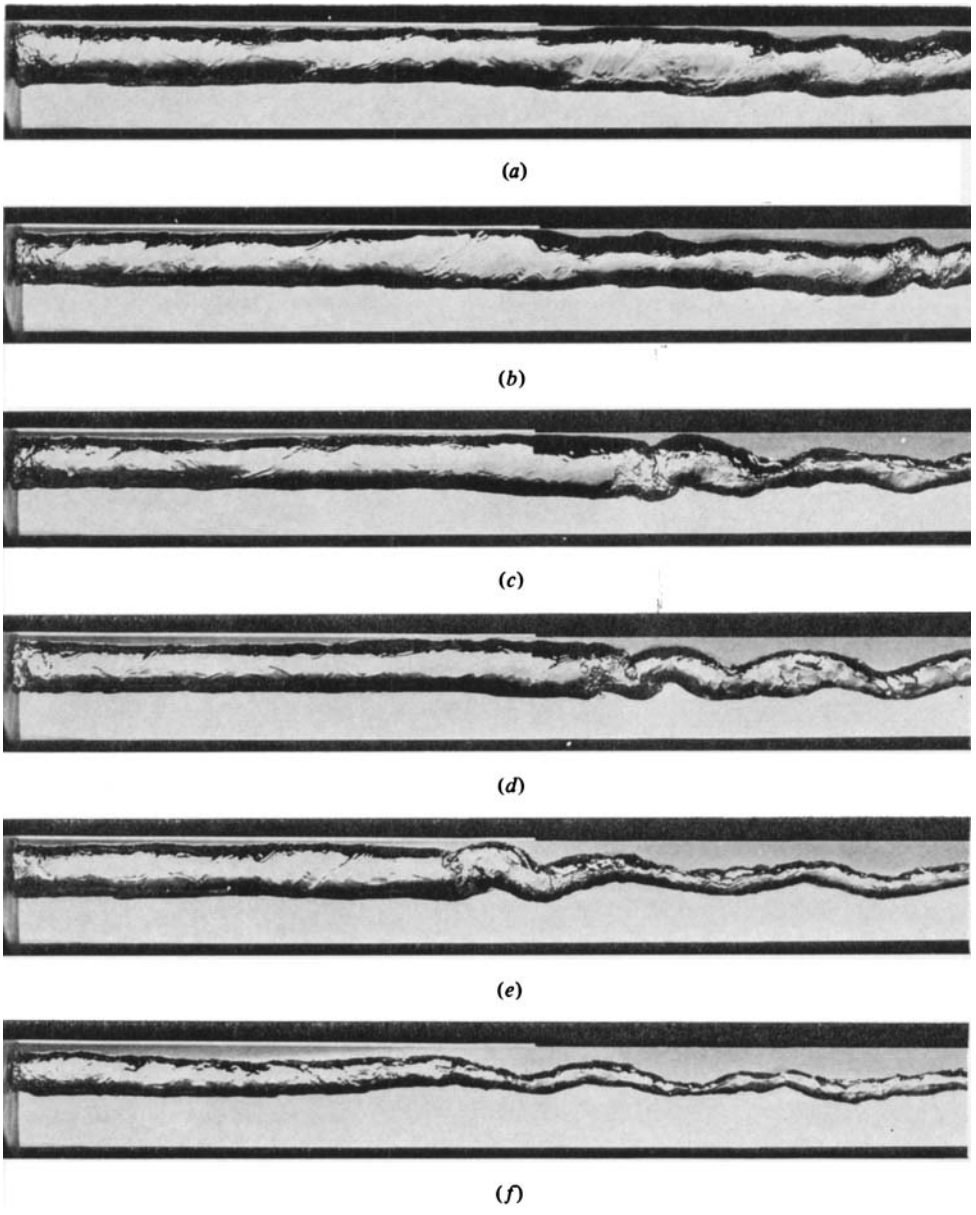

FIGURE 13. Photographs of hollow vortex core in 55 mm diameter tube. Inlet-slit length is 210 mm; flow rate is 5·2 l s^{-1}.

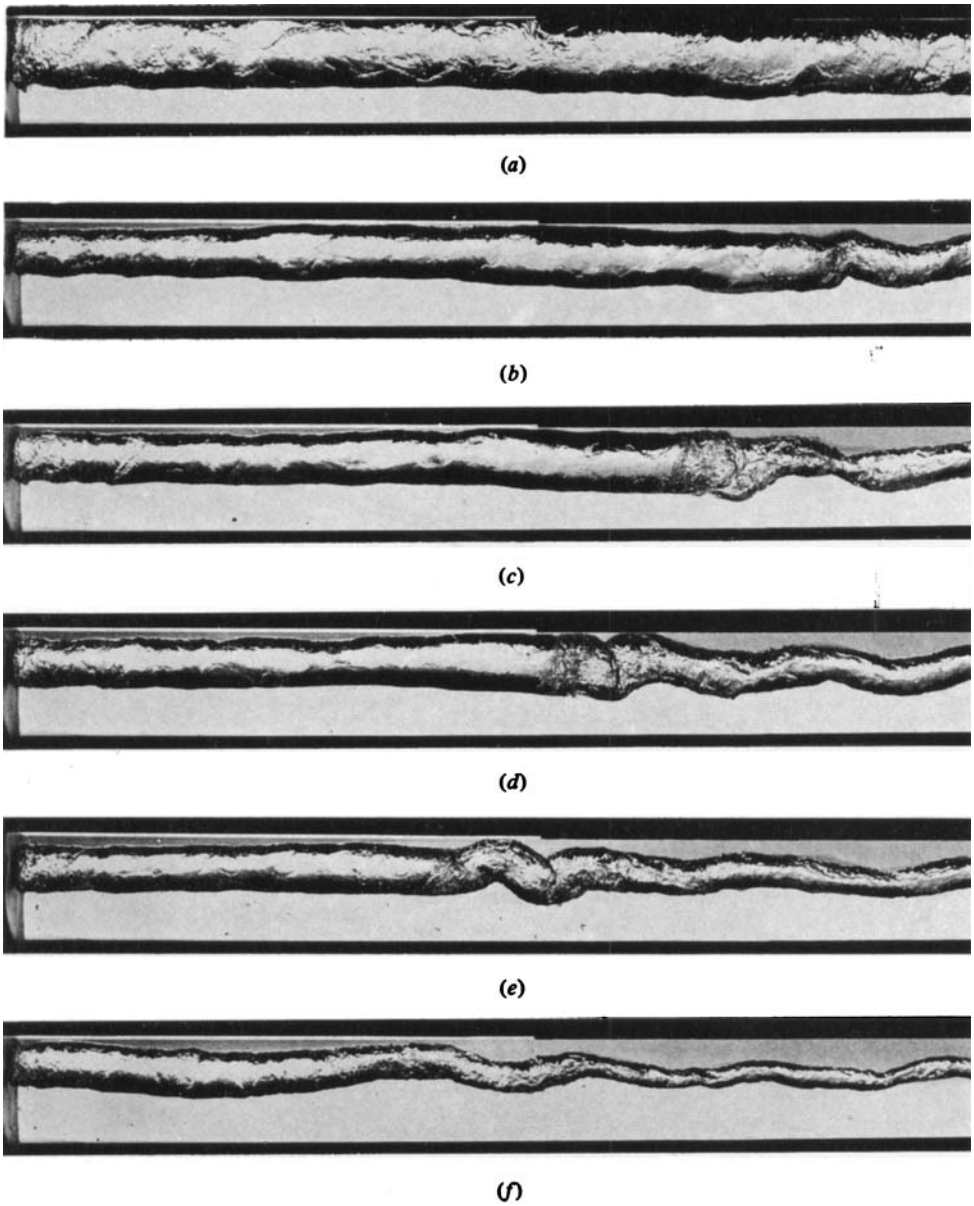

FIGURE 14. Photographs of hollow vortex core in 55 mm diameter tube. Inlet-slit length is 210 mm; flow rate is 2·04 l s^{-1}.

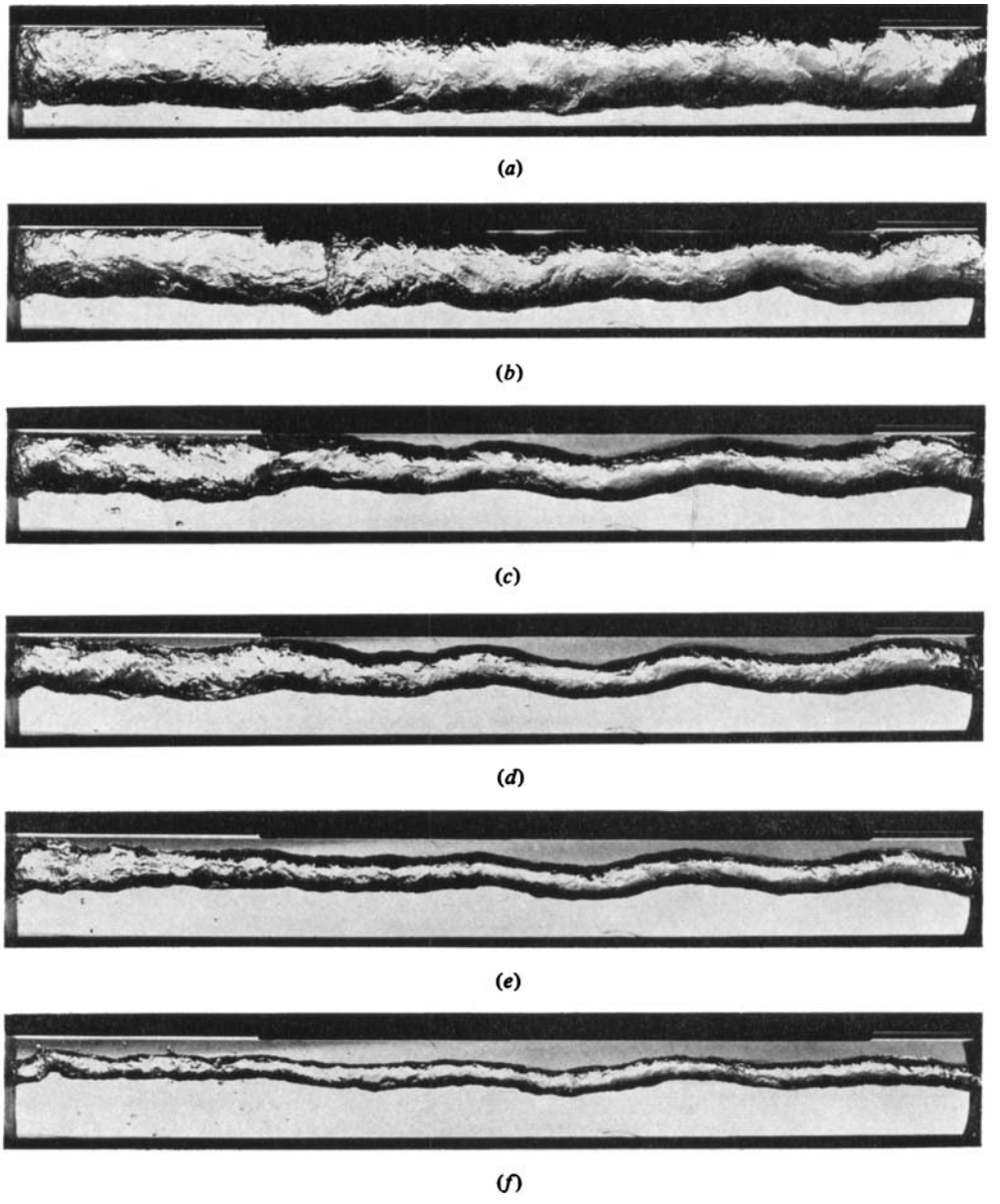

FIGURE 15. Photographs of hollow vortex core in 55 mm diameter tube. Inlet-slit length is 100 mm; flow rate is 4·1 l s^{-1}.